

Communication

A Highly Active Au/In₂O₃-ZrO₂ Catalyst for Selective Hydrogenation of CO₂ to Methanol

Zhe Lu, Kaihang Sun, Jing Wang, Zhitao Zhang and Changjun Liu * 

School of Chemical Engineering and Technology, Tianjin University, Tianjin 300072, China; rollingro@tju.edu.cn (Z.L.); kaihangsun@tju.edu.cn (K.S.); wangjing102@tju.edu.cn (J.W.); zhang_zhitao@tju.edu.cn (Z.Z.)

* Correspondence: cjl@tju.edu or ughg_cjl@yahoo.com; Tel.: +86-22-27406490

Received: 29 October 2020; Accepted: 20 November 2020; Published: 23 November 2020

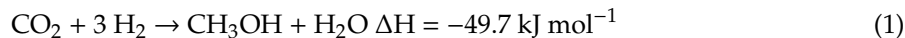


Abstract: A novel gold catalyst supported by In₂O₃-ZrO₂ with a solid solution structure shows a methanol selectivity of 70.1% and a methanol space–time yield (STY) of 0.59 g_{MeOH} h⁻¹ g_{cat}⁻¹ for CO₂ hydrogenation to methanol at 573 K and 5 MPa. The ZrO₂ stabilizes the structure of In₂O₃, increases oxygen vacancies, and enhances CO₂ adsorption, causing the improved activity.

Keywords: CO₂ hydrogenation; indium oxide; Au/In₂O₃-ZrO₂; methanol; solid solution

1. Introduction

With the development of renewable hydrogen, hydrogenation of CO₂ to methanol (Equation (1)) has received increasing attention worldwide. Significant efforts have been made towards the preparation of catalysts with high CO₂ conversion and high methanol selectivity. The most investigated catalysts are promoted copper catalysts based on the industrial Cu/ZnO catalysts for methanol synthesis from syngas [1–3]. Recently, ZnO-ZrO₂ [4], GaNi alloy [5], bimetallic PdZn [6], MOF [7,8], and others [1] were reported to have nice activity for CO₂ hydrogenation to methanol.



In 2012, our group predicted via density functional theoretical (DFT) studies that In₂O₃ possesses high activity for CO₂ activation [9]. The further DFT [10] and experimental [11] studies confirmed that In₂O₃ with oxygen vacancies exhibited high activity for CO₂ hydrogenation to methanol, with unusually high methanol selectivity. Since then, In₂O₃-based catalysts have received significant attention, with increasing publications. The reported works include preparation and characterization of In₂O₃ [12]; combination of In₂O₃ with other oxides [13,14], especially ZrO₂ that forms the solid solution with In₂O₃ and improves CO₂ adsorption with optimum oxygen vacancy [15–17] and generates strong electronic interaction between oxides [18]; and the addition of metals, including gold [19,20], copper [21,22], cobalt [23], palladium [24–27], rhodium [28], nickel [29], and platinum [30,31]. The metal catalysts applied significantly improve the hydrogenation ability of In₂O₃. It has been found that In₂O₃ has a strong interaction with metals. This strong interaction causes a total change in catalytic performance. It makes the Ni, Au, Rh, and Pt catalysts become highly selective towards CO₂ hydrogenation to methanol with In₂O₃ support. Especially for the Au catalyst, most of the reported Au catalysts are highly active for oxidation, with almost a thousand papers per year recently. However, only a few papers were published for hydrogenation. The In₂O₃-supported Au catalyst shows the highest selectivity and best activity ever reported for CO₂ hydrogenation to methanol. The methanol selectivity reaches 100% at temperatures below 498 K and is more than 70% at 548 K [19]. It is even 67.8% at 573 K, with a space–time yield (STY) of methanol of 0.47 g_{MeOH} h⁻¹ g_{cat}⁻¹ at 573 K, 5 MPa, and 21,000 cm³ h⁻¹ g_{cat}⁻¹.

In this work, we confirm that the In_2O_3 - ZrO_2 supported Au catalyst presents even higher activity for CO_2 hydrogenation to methanol.

2. Results

In_2O_3 - ZrO_2 oxides were prepared via a co-precipitation method, and then Au nanoparticles (NPs) were loaded on the carrier through the deposition–precipitation method. The loading amount of Au was 1%. The samples after reaction at 573 K and 5 MPa were named with “-AR” at the end. As shown in Supplementary Materials Figure S1, the sample with In/Zr molar ratio of 4:1 shows the best catalytic performance. The sample with this In/Zr ratio (labeled as $\text{Au}/\text{In}_2\text{O}_3$ - ZrO_2) was thus selected for the activity test and further characterization. Based on the N_2 adsorption–desorption test on 77 K, the In_2O_3 - ZrO_2 and $\text{Au}/\text{In}_2\text{O}_3$ - ZrO_2 samples exhibit a similar total specific surface area of 111.5 and $121.6 \text{ m}^2 \text{ g}^{-1}$, respectively. As shown in Figure 1a, the results of X-ray diffraction (XRD) show that the characterized peaks for all samples containing indium belong to cubic- In_2O_3 (PDF file number 06-0416). Meanwhile, the peaks corresponding to Au cannot be observed, which results from the extremely low loading and ultra-high dispersion of Au NPs. This also means that Au NPs remain stable, preventing deactivation by the agglomeration. The absence of metallic indium after reaction also shows that the structure of the $\text{Au}/\text{In}_2\text{O}_3$ - ZrO_2 catalyst is stable during the reaction. Moreover, the diffraction peak of the In_2O_3 - ZrO_2 sample largely differentiates from that of ZrO_2 , which can be deduced that Zr may be penetrated into In_2O_3 [32]. In Figure 1b, the high-resolution transmission electron microscopy (HRTEM) image of the $\text{Au}/\text{In}_2\text{O}_3$ - ZrO_2 sample shows the crystalline lattice distances of 0.180, 0.398, 0.275, and 0.291 nm, which are assigned to cubic- In_2O_3 (440), (211), (321), and (222) facets, respectively. No lattice fringes of ZrO_2 or Au can be observed. As shown in Figure 1c, the result of element distribution analysis indicates that the supported Au NPs and Zr are highly dispersed before and after reaction (Supplementary Materials Figure S2). These results further confirm the excellent dispersion of Au NPs and the conclusion that In_2O_3 - ZrO_2 is in a solid solution state.

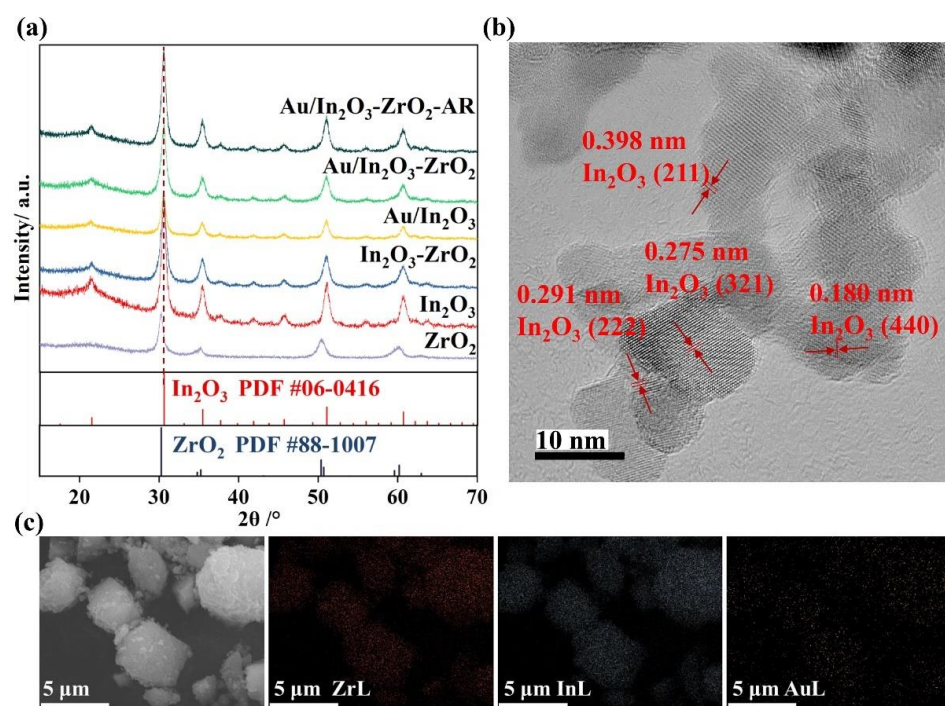


Figure 1. (a) XRD patterns of various oxides and Au-supported oxides; (b) HRTEM image of $\text{Au}/\text{In}_2\text{O}_3$ - ZrO_2 ; (c) scanning electron microscope (SEM) image and corresponding energy-dispersive X-ray spectroscopy (EDX) mapping of $\text{Au}/\text{In}_2\text{O}_3$ - ZrO_2 .

The activity test of CO₂ hydrogenation to methanol was conducted in a vertical fixed-bed reactor. The products were analyzed with an online gas chromatograph (Agilent 7890A). For all catalysts, methanol and CO are the main products. Trace methane can be detected at reaction temperatures over 548 K. The carbon balance is better than 99%. As shown in Figure 2a, the Au/In₂O₃-ZrO₂ catalyst exhibits the highest catalytic performance among these three catalysts. The CO₂ conversion of the Au/In₂O₃-ZrO₂ catalyst is 14.8% at 573 K and 5 MPa. The methanol STY reaches 0.59 g_{MeOH} h⁻¹ g_{cat}⁻¹, which is much higher than that over the Au/In₂O₃ catalyst (0.47 g_{MeOH} h⁻¹ g_{cat}⁻¹) [19] and other Au-based catalysts (Supplementary Materials Table S1). For all catalysts, CO₂ conversion increases with the temperature increases, while the methanol selectivity decreases due to the competitive reverse water–gas shift (RWGS) reaction (Equation (2)). Although CO can be detected at 498 K for the Au/In₂O₃-ZrO₂ catalyst, the higher methanol selectivity at 523 K and 548 K is obvious, as compared to the Au/In₂O₃ catalyst. This result reveals that the Au/In₂O₃-ZrO₂ catalyst maintains high selectivity for methanol synthesis from CO₂ hydrogenation. On the other hand, the presence of Zr enhances the CO₂ conversion of the Au/In₂O₃ catalysts. As shown in Figure 2c, the methanol STY on the Au/In₂O₃-ZrO₂ catalyst only decreases slightly and is stabilized at 92% of the initial value after a 6 h reaction at 573 K and 5 MPa. Furthermore, the Au/In₂O₃-ZrO₂ catalyst shows the lowest apparent activation energy (E_a) of 74.1 kJ mol⁻¹ (Figure 2d). These results prove the excellent performance for CO₂ hydrogenation to methanol over the Au/In₂O₃-ZrO₂ catalyst.

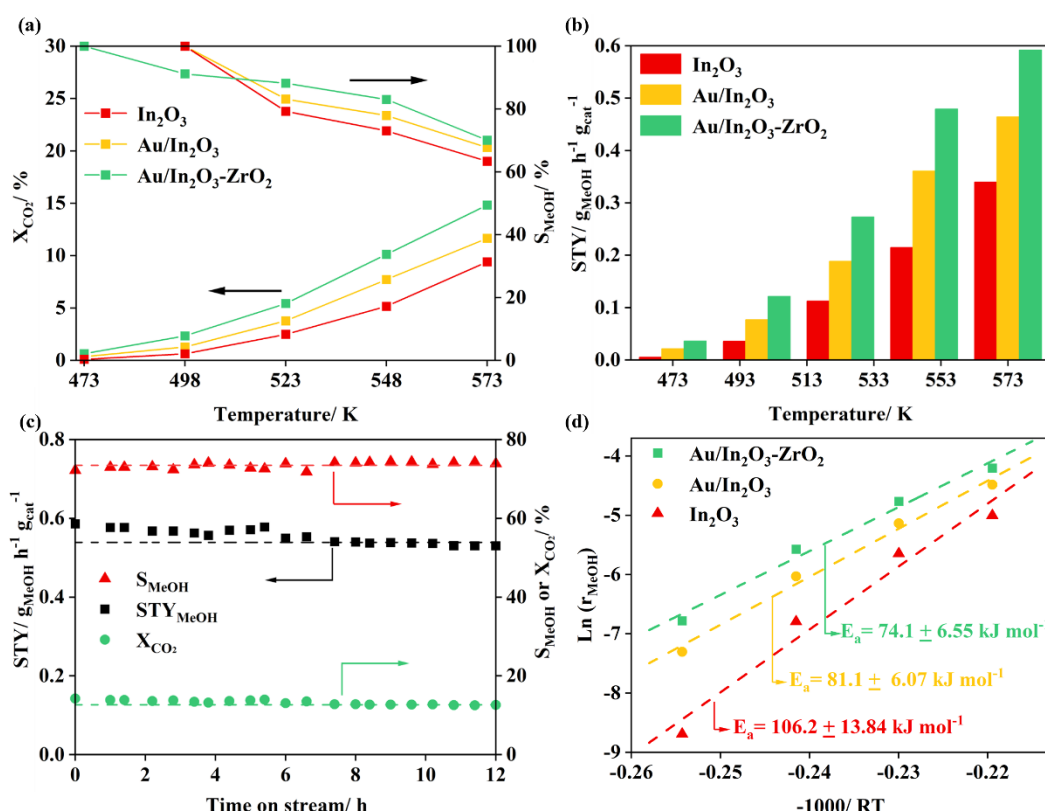
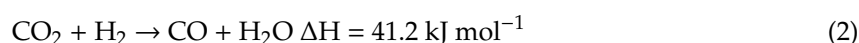


Figure 2. Comparison of (a) CO₂ conversion and methanol selectivity, and (b) methanol space–time yield (STY) over the In₂O₃, Au/In₂O₃, and Au/In₂O₃-ZrO₂ catalysts as a function of temperature; (c) CO₂ conversion, methanol selectivity, and methanol STY versus time of the Au/In₂O₃-ZrO₂ catalyst on stream (TOS); (d) Arrhenius plots for methanol production over the In₂O₃, Au/In₂O₃, and Au/In₂O₃-ZrO₂ catalysts. (Reaction conditions: 5.0 MPa, H₂/CO₂/N₂ = 76/19/5, GHSV = 21,000 cm³ h⁻¹ g_{cat}⁻¹).

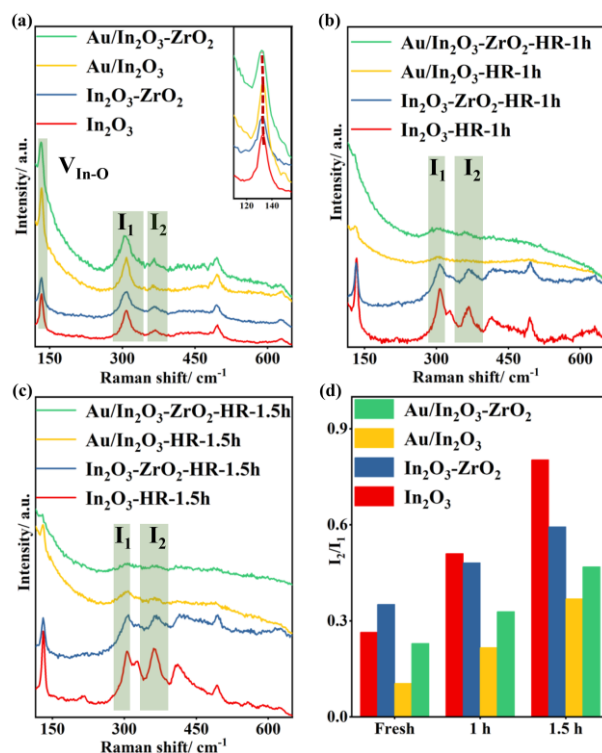


Figure 3. Visible Raman spectra of fresh samples (**a**) with the inset showing the enlargement of Raman spectra around 140 cm^{-1} , and the samples after hydrogen reduction for 1 h (**b**) and 1.5 h (**c**); the comparison of the relative amount of the oxygen vacancies according to I_2/I_1 value (**d**). (H_2 reduction conditions: 473 K, 0.1 MPa, 10% H_2/Ar .)

To further understand the factors responsible for the enhanced catalytic performance, Raman analyses were performed. As shown in Figure 3a, the band at 132 cm^{-1} is assigned to the In-O vibration ($V_{\text{In}-\text{O}}$) [25]. The scattering features at 306 cm^{-1} (I_1) and 493 cm^{-1} belong to the bending vibration and stretching vibrations of InO_6 octahedrons, respectively [33]. The stretching vibration of In-O-In, occurring at 364 cm^{-1} (I_2), was confirmed to reflect the degree of oxygen defects [19]. For fresh samples, the band of $V_{\text{In}-\text{O}}$ visibly shifts towards lower frequencies due to the addition of Zr. Moreover, the characteristic peaks of the $\text{In}_2\text{O}_3\text{-ZrO}_2$ and $\text{Au}/\text{In}_2\text{O}_3\text{-ZrO}_2$ samples are completely the same as those of In_2O_3 without the peaks attributed to ZrO_2 (Supplementary Materials Figure S3). These results affirm the penetration of Zr atoms into the indium oxides [32]. The intensities of I_2 increase with the addition of Zr, suggesting that more oxygen vacancies are generated. However, the loading of Au results in lower I_2 intensities, likely owing to the coverage of Au NPs on oxygen vacancies [30]. Subsequently, the variation of related peaks over the samples after H_2 reduction for different times under 473 K (labeled with “-HR-1.5h” or “-HR-1h” at the end) was further investigated. As shown in Figure 3b,c, H_2 reduction results in the increase of oxygen vacancies for all samples, according to the much larger I_2 band [30]. Moreover, prolonging reduction time enables oxygen vacancies to increase sequentially. The area ratio of I_2 and I_1 (labeled as I_2/I_1) was calculated to characterize the amount of oxygen vacancies (Figure 3d). The oxygen vacancies of the $\text{Au}/\text{In}_2\text{O}_3$ sample are 40% of fresh In_2O_3 , while those of the $\text{Au}/\text{In}_2\text{O}_3\text{-HR-1.5h}$ sample are 46% of the $\text{In}_2\text{O}_3\text{-HR-1.5h}$ sample. Comparing $\text{Au}/\text{In}_2\text{O}_3\text{-ZrO}_2$ with $\text{In}_2\text{O}_3\text{-ZrO}_2$ under the same treatment condition, we see that the ratio of their I_2/I_1 value increases by 21% from fresh samples to the samples after 1.5 h H_2 reduction. This result indicates that the well-dispersed Au NPs benefit the formation of oxygen vacancies under the atmosphere including H_2 . Furthermore, normalized by the I_2/I_1 value of fresh In_2O_3 , the oxygen vacancies of samples after 1.5 h H_2 reduction increase by 2.04, 0.92, 1.00, and 0.90 times in In_2O_3 , $\text{In}_2\text{O}_3\text{-ZrO}_2$, $\text{Au}/\text{In}_2\text{O}_3$, and $\text{Au}/\text{In}_2\text{O}_3\text{-ZrO}_2$, respectively. During the H_2 reduction process, the oxygen

vacancies of In_2O_3 increase much more drastically than the other samples. Noticeably, some bulk information of the sample can be obtained under the excitation laser with the wavelength of 532 nm [34]. The rapid increment of oxygen vacancies can be attributed to the over-reduction of pure In_2O_3 [30]. It results in metallic indium without activity for H_2 activation [13]. Thus, it can be deduced that the strong metal-support interaction (SMSI) between Au and carriers could be conducive to maintain the structure of In_2O_3 [19], which can also be performed through the incorporation of Zr into In_2O_3 . Furthermore, compared to $\text{Au}/\text{In}_2\text{O}_3$, the $\text{Au}/\text{In}_2\text{O}_3\text{-ZrO}_2$ sample exhibits the higher I_2/I_1 values for not only fresh samples but also the samples after reduction, implying the increase of oxygen vacancy density. These results coincide with the better catalytic activity of the $\text{Au}/\text{In}_2\text{O}_3\text{-ZrO}_2$ catalyst.

H_2 temperature-programmed reduction ($\text{H}_2\text{-TPR}$) was employed to investigate the reduction behaviors of the catalysts. The $\text{H}_2\text{-TPR}$ profiles are shown in Figure 4a. For all samples, the reduction peaks located below 500 K can be assigned to the surface reduction [30]. The onset of reduction peak at 530 K belongs to the reduction of bulk In_2O_3 . Due to the fact that In_2O_3 can be reduced by hydrogen more easily than ZrO_2 [17], the enhanced stability of $\text{Au}/\text{In}_2\text{O}_3\text{-ZrO}_2$ under the hydrogen atmosphere is thereby achieved. The XRD patterns of the spent samples were further investigated. As shown in Supplementary Materials Figure S4, there is a noticeable shift towards a lower angle for the $\text{In}_2\text{O}_3\text{-AR}$ sample compared to fresh In_2O_3 , while the $\text{Au}/\text{In}_2\text{O}_3$ and $\text{Au}/\text{In}_2\text{O}_3\text{-ZrO}_2$ samples can remain at the same angle after the reaction at 573 K and 5 MPa. Our previous work reported that the lattice expansion of In_2O_3 caused by thermal effect and oxygen vacancies could be performed on the shift of XRD diffraction peak [19]. Moreover, it is similar for lattice parameters of In_2O_3 and $\text{Au}/\text{In}_2\text{O}_3$, heated under argon and reactant mixture at 573 K, respectively [19]. As the thermal effect can be excluded, it can be conducted that this shift may be attributed to the increasing oxygen vacancies of bulk In_2O_3 . Thus, it can be deduced that the addition of Zr and Au could effectively hinder the over-reduction of In_2O_3 under a reactant mixture including H_2 . In the temperature range from 275 to 530 K, the surface reduction peak shifts towards the lower temperature (below 360 K) with the addition of Au NPs. This result confirms that Au NPs promote the formation of surface oxygen vacancies. In addition, a broader and intense H_2 consumption peak at 350 K for the $\text{Au}/\text{In}_2\text{O}_3\text{-ZrO}_2$ sample is obvious. The incorporation of Zr into In_2O_3 promotes the formation of surface oxygen vacancies on the $\text{Au}/\text{In}_2\text{O}_3\text{-ZrO}_2$ sample. The higher onset temperature of surface reduction and the disappeared peak at 456 K indicate the stabilization function of Zr on In_2O_3 structure. These results are in line with the results of Raman spectra above. The $\text{H}_2\text{-TPR}$ profiles demonstrate the increasing surface oxygen vacancies over the $\text{Au}/\text{In}_2\text{O}_3\text{-ZrO}_2$ catalyst, as a reason for its prominent catalytic activity.

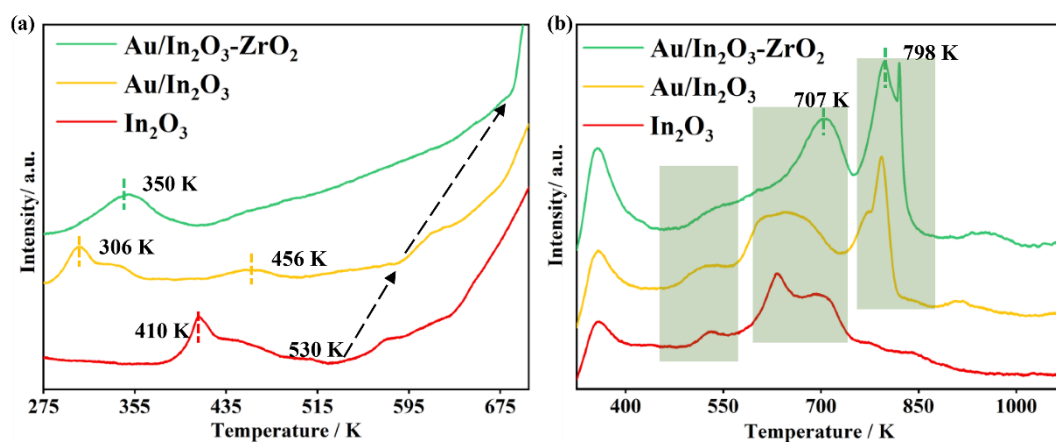


Figure 4. $\text{H}_2\text{-TPR}$ profiles (a) and $\text{CO}_2\text{-TPD}$ profiles (b) of In_2O_3 and Au-supported oxides.

To further investigate the adsorption behavior of CO_2 on the catalyst surface, temperature-programmed desorption of CO_2 ($\text{CO}_2\text{-TPD}$) was conducted. Figure 4b presents the profiles of $\text{CO}_2\text{-TPD}$, involving several signals in the temperature ranges of 325–425, 485–570, 570–755, and 730–865 K. The single peak around

360 K for all samples belongs to the desorption of physically absorbed CO₂ [35]. Other peaks from low to high temperatures can be attributed to chemically adsorbed CO₂ on the different sites, ascribed to weak, medium, and strong basic sites, respectively. Comparing the Au/In₂O₃-ZrO₂ sample with other samples, we see that the desorption peaks shift to the much higher temperatures of 707 and 798 K, respectively. This result implies that the addition of Zr enhances the strength of CO₂ adsorption on these sites, probably owing to the enhanced basicity [36]. It can be proposed that the enhanced CO₂ adsorption on the Au/In₂O₃-ZrO₂ sample benefits methanol synthesis. Time-resolved in situ diffuse reflectance infrared Fourier transform spectroscopy (in situ DRIFTS) were also conducted to gain the insights into CO₂ adsorption. As shown in Supplementary Materials Figure S5, the CO₂ interaction with Au/In₂O₃-ZrO₂ prefers to produce carbonate species rather than bicarbonate species due to the change of intensities [37]. The bicarbonate species disappears much faster after the Ar desorption, especially over the Au/In₂O₃ sample. Moreover, compared to the Au/In₂O₃ sample, the blue shift over the Au/In₂O₃-ZrO₂ sample for the bands at 900–1100 cm⁻¹, attributed to CO₂ absorbed on vacancies, suggests the stronger adsorption of CO₂ [17,38]. These results reveal that the addition of Zr strengthens the interaction between CO₂ and the catalyst surface. Based on the discussion above, the SMSI between Au and In₂O₃-ZrO₂ solid solution facilitates H₂ dissociation. Meanwhile, the incorporation of Zr into In₂O₃ leads to the increasing oxygen vacancies, as well as the enhanced CO₂ adsorption. The H adatoms, dissociated by the Au NPs strongly interacting with the carrier, can spill over to the oxygen vacancy sites and react with the CO₂ molecule activated on the oxygen vacancy sites. This significantly promotes the CO₂ conversion into methanol.

In conclusion, we have shown that the integration of Au, In₂O₃, and ZrO₂ enables the high selectivity for methanol synthesis from CO₂ hydrogenation. The Au/In₂O₃-ZrO₂ catalyst shows a CO₂ conversion of 14.8% with a methanol STY of 0.59 g_{MeOH} h⁻¹ g_{cat}⁻¹ at 573 K and 5 MPa. Such an outstanding activity indicates that the addition of Zr remarkably improves the activity of the Au/In₂O₃ catalyst. The catalyst characterizations demonstrate that Au NPs are well dispersed on the surface of the In₂O₃-ZrO₂ solid solution. Further investigation through Raman spectra, H₂-TPR, and CO₂-TPD indicates that the enhanced H₂ activation is achieved by the Au NPs strongly interacting with catalysts surface due to the SMSI effect. The presence of Zr mainly exhibits four effects: (1) reducing the apparent activation energy, (2) stabilizing the structure of In₂O₃, (3) increasing the amount of oxygen vacancies, and (4) enhancing the CO₂ adsorption. This work not only extends the utilization of gold catalysts for CO₂ hydrogenation but also promotes the fundamental studies for CO₂ conversion.

3. Materials and Methods

3.1. Catalyst Preparation

Indium-zirconium oxide carriers were prepared by a co-precipitation approach. Appropriate amounts of In(NO₃)₃·xH₂O (M = 363.3 g mol⁻¹, Beijing HWRK Chem Co., Ltd., Beijing, China, 99.99%) and ZrO(NO₃)₂·xH₂O (M = 257.9 g mol⁻¹, Shanghai Macklin Biochemicals Co., Ltd., Shanghai, China, 99%) with a fixed molar ratio were firstly dissolved in deionized water (0.145 M of In³⁺). A 0.2 M aqueous solution of Na₂CO₃ (Tianjin Kemiou Chemical Reagent Co., Ltd., Tianjin, China, 99%) was added dropwise under continuous stirring to reach a pH of 10. The mixture was aged at 353 K for 3 h. Thereafter, the precipitate was filtered and then washed with deionized water several times. Prior to the calcination at 723 K (10 K min⁻¹, 3 h), the sample was dried at 353 K overnight. The obtained carrier was labeled as In₂O₃-ZrO₂. The In₂O₃ and ZrO₂ samples were prepared with the same protocol. The Au/In₂O₃-ZrO₂ sample was prepared via a deposition-precipitation method, which is described in detail elsewhere [19]. The only difference was that the sample after freeze-drying overnight was directly used for the catalytic activity test, without a further reduction step. The samples with other molar ratios of In/Zr were denoted as Au/In₂O₃-ZrO₂ (m:n), where m:n is the molar ratio of In/Zr.

3.2. Characterization

The phase compositions of the samples were characterized by a Bruker D8 Focus diffractometer equipped with Cu K α radiation source ($\lambda = 1.54056 \text{ \AA}$). Diffraction data were collected at a scanning speed of 8° min^{-1} over the 2θ range of 10° – 70° . The N₂ adsorption/desorption isotherms, measuring on an AUTOSORB-1-C instrument (Quantachrome) at 77 K, were used to determine the total specific surface area (S_{BET}).

The Raman spectra were recorded by an INVIA Raman analyzer (Renishaw PLC. Ltd., Gloucestershire, UK) with laser irradiation at 532 nm. The SEM images and EDX spectra were used to characterize microstructure and element distribution. All samples were measured on a Hitachi S-4800 SEM at an operating voltage of 25 kV without any conductive coating process. The transmission electron microscopy (TEM) and HRTEM images were obtained using a JEOL JEM-F200 microscope at the accelerating voltage of 200 kV.

H₂-TPR was carried out using the Micromeritics Autochem II 2920 chemisorption analyzer. About 100 mg of the as-prepared sample was pretreated under flowing helium for 1 h at 473 K to remove the absorbed impurities. Thereafter, the sample was cooled down to 273 K by liquid nitrogen under flowing helium. Then the sample was heated to 973 K (10 K min^{-1}) after switching to a mixture gas of 10% H₂ in N₂. The effluent gas was analyzed using a thermal conductivity detector (TCD). The signals were normalized to the weight of the sample for the following analysis.

CO₂-TPD was conducted on the same apparatus as H₂-TPR. After the same pretreating process as H₂-TPR, the sample (about 100 mg) was cooled down to 323 K under flowing helium, followed by CO₂ adsorption for 1 h. After being purged with flowing helium for 1 h to remove physically absorbed CO₂ at the same temperature, the sample was heated to 1073 K under flowing helium at a rate of 10 K min^{-1} . The effluent gas was analyzed by the TCD. The signals were normalized to the weight of the sample for the following analysis.

Time-resolved in situ DRIFTS was performed using a Tensor 27 spectrometer (Bruker) equipped with a MCT detector by recording 32 scans at a resolution of 2 cm^{-1} . After the pretreatment under flowing argon for 2 h at 323 K, the background spectra were firstly collected and subtracted from the sample spectra. For CO₂ adsorption, a 1.0% CO₂ in Ar gas with the flow rate of 20 mL min^{-1} was fed into the system at 323 K. After the collecting of time-resolved spectra for 30 min, the gas was switched to pure Ar. The desorption time-resolved spectra were collected after flushing for 10 min.

3.3. Catalyst Activity Test

The activity test of CO₂ hydrogenation to methanol was conducted in a vertical fixed-bed reactor setup. The reactor was loaded with 0.2 g of the catalysts and 1.0 g of SiC, which was purged with N₂, at room temperature. After 0.5 h, the gas flow was switched to the reactant mixture (H₂/CO₂/N₂ = 76/19/5, molar ratio) until the pressure reached 5 MPa. The reaction was conducted with a temperature range from 473 to 573 K. The gaseous hourly space velocity (GHSV) was $21,000 \text{ cm}^3 \text{ h}^{-1} \text{ g}_{\text{cat}}^{-1}$. The reaction conditions were determined by the reported studies [17,39] and our previous study on Au/In₂O₃ [19] in order to get better catalytic performance. Products were analyzed with an online gas chromatograph (Agilent 7890A) equipped with a flame ionized detector (FID) and a TCD. All the valves and lines between the reactor outlet and GC inlet were heated to 413 K to prevent the condensation of methanol. CO₂ conversion (X_{CO₂}) and selectivity (S_i) and space-time yield (STY, $\text{g}_i \text{ g}_{\text{cat}}^{-1} \text{ h}^{-1}$) of product i (i = methanol or CO) were calculated as follows:

$$X_{\text{CO}_2} = (F_{\text{CO}_2, \text{in}} - F_{\text{CO}_2, \text{out}})/F_{\text{CO}_2, \text{in}} \times 100\%$$

$$S_i = F_{i, \text{out}}/(F_{\text{CO}_2, \text{in}} - F_{\text{CO}_2, \text{out}}) \times 100\%$$

$$\text{STY}_i = (F_{\text{CO}_2, \text{in}} \times S_i \times X_{\text{CO}_2})/m_{\text{cat}} \times M_i$$

where F and M are the molar flow rate and the molar mass of product i , respectively, and m_{cat} is the catalyst sample weight.

Supplementary Materials: The following are available online at <http://www.mdpi.com/2073-4344/10/11/1360/s1>. Table S1: Comparison of Au catalysts for CO₂ hydrogenation to methanol. Figure S1: (a) CO₂ conversion and methanol selectivity, and (b) methanol space–time yield (STY) respect to the molar In content, which is equal to $m/(m+n)$ for the Au/In₂O₃-ZrO₂ (m:n) sample. Reaction conditions: 5 MPa, H₂/CO₂/N₂ = 76/19/5, GHSV = 21,000 cm³ h⁻¹ g_{cat}⁻¹. Figure S2: TEM images of Au/In₂O₃-ZrO₂ (a), Au/In₂O₃-ZrO₂-AR (b) and Au/In₂O₃-ZrO₂-AR (c); SEM image (d) and the corresponding EDX mapping of Au/In₂O₃-ZrO₂-AR. Figure S3: Visible Raman spectra of fresh ZrO₂, Au/In₂O₃-ZrO₂, In₂O₃-ZrO₂, and In₂O₃. Figure S4: Enlarged XRD patterns of peaks around 32° for fresh samples and the samples after reaction. Figure S5: Time-resolved in situ DRIFTS as a function of CO₂ adsorption time and Ar desorption time at 323 K after pretreatment in Ar over Au/In₂O₃ (a) and Au/In₂O₃-ZrO₂ (b). Symbol definition: bicarbonate (white frame), carbonate (red frame), CO₂ absorbed on the vacancies featuring the higher CO₂ adsorption energy (yellow frame).

Author Contributions: C.L., conceptualization, supervision, and review and revision of the final version of the paper; Z.L., investigation, methodology, and visualization and writing—original draft preparation; K.S., methodology, and review and editing; J.W., review and editing; Z.Z., visualization. All authors have read and agreed to the published version of the manuscript.

Funding: This work was supported by the National Key Research and Development Program of China (2016YFB0600902).

Conflicts of Interest: The authors declare no conflict of interest.

References

1. Jiang, X.; Nie, X.; Guo, X.; Song, C.; Chen, J.G. Recent advances in carbon dioxide hydrogenation to methanol via heterogeneous catalysis. *Chem. Rev.* **2020**, *120*, 7984–8034.
2. Wang, W.; Wang, S.; Ma, X.; Gong, J. Recent advances in catalytic hydrogenation of carbon dioxide. *Chem. Soc. Rev.* **2011**, *40*, 3703–3727.
3. Su, X.; Xu, J.; Liang, B.; Duan, H.; Hou, B.; Huang, Y. Catalytic carbon dioxide hydrogenation to methane: A review of recent studies. *J. Energy Chem.* **2016**, *25*, 553–565.
4. Wang, J.; Li, G.; Li, Z.; Tang, C.; Feng, Z.; An, H.; Liu, H.; Liu, T.; Li, C. A highly selective and stable ZnO-ZrO₂ solid solution catalyst for CO₂ hydrogenation to methanol. *Sci. Adv.* **2017**, *3*, e1701290.
5. Studt, F.; Sharafutdinov, I.; Abild-Pedersen, F.; Elkjaer, C.F.; Hummelshøj, J.S.; Dahl, S.; Chorkendorff, I.; Nørskov, J.K. Discovery of a Ni-Ga catalyst for carbon dioxide reduction to methanol. *Nat. Chem.* **2014**, *6*, 320–324.
6. Liao, F.; Wu, X.-P.; Zheng, J.; Li, M.M.-J.; Kröner, A.; Zeng, Z.; Hong, X.; Yuan, Y.; Gong, X.-Q.; Tsang, S.C.E. A promising low pressure methanol synthesis route from CO₂ hydrogenation over Pd@Zn core–shell catalysts. *Green Chem.* **2017**, *19*, 270–280.
7. Xiang, W.; Zhang, Y.; Chen, Y.; Liu, C.J.; Tu, X. Synthesis, characterization and application of defective metal–organic frameworks: Current status and perspectives. *J. Mater. Chem. A* **2020**, *8*, 21526–21546.
8. Gutterød, E.S.; Lazzarini, A.; Fjermestad, T.; Kaur, G.; Manzoli, M.; Bordiga, S.; Svelle, S.; Lillerud, K.P.; Skúlason, E.; Øien-Ødegaard, S.; et al. Hydrogenation of CO₂ to methanol by Pt nanoparticles encapsulated in UiO-67: Deciphering the role of the metal–organic framework. *J. Am. Chem. Soc.* **2020**, *142*, 999–1009. [PubMed]
9. Ye, J.; Liu, C.; Ge, Q. DFT study of CO₂ adsorption and hydrogenation on the In₂O₃ surface. *J. Phys. Chem. C* **2012**, *116*, 7817–7825.
10. Ye, J.; Liu, C.; Mei, D.; Ge, Q. Active oxygen vacancy site for methanol synthesis from CO₂ hydrogenation on In₂O₃(110): A DFT Study. *ACS Catal.* **2013**, *3*, 1296–1306.
11. Sun, K.; Fan, Z.; Ye, J.; Yan, J.; Ge, Q.; Li, Y.; He, W.; Yang, W.; Liu, C.-J. Hydrogenation of CO₂ to methanol over In₂O₃ catalyst. *J. CO₂ Util.* **2015**, *12*, 1–6.
12. Tsoukalou, A.; Abdala, P.M.; Stoian, D.; Huang, X.; Willinger, M.-G.; Fedorov, A.; Müller, C.R. Structural evolution and dynamics of an In₂O₃ catalyst for CO₂ hydrogenation to methanol: An operando XAS-XRD and in situ TEM study. *J. Am. Chem. Soc.* **2019**, *141*, 13497–13505. [PubMed]
13. Chen, T.-Y.; Cao, C.; Chen, T.-B.; Ding, X.; Huang, H.; Shen, L.; Cao, X.; Zhu, M.; Xu, J.; Gao, J.; et al. Unraveling highly tunable selectivity in CO₂ hydrogenation over bimetallic In-Zr oxide catalysts. *ACS Catal.* **2019**, *9*, 8785–8797.

14. Dou, M.; Zhang, M.; Chen, Y.; Yu, Y. Mechanistic insight into the modification of the surface stability of In_2O_3 catalyst through metal oxide doping. *Catal. Lett.* **2018**, *148*, 3723–3731.
15. Tsoukalou, A.; Abdala, P.M.; Armutlulu, A.; Willinger, E.; Fedorov, A.; Müller, C.R. Operando X-ray absorption spectroscopy identifies a monoclinic ZrO_2 : In solid solution as the active phase for the hydrogenation of CO_2 to methanol. *ACS Catal.* **2020**, *10*, 10060–10067.
16. Frei, M.S.; Mondelli, C.; Cesarin, A.; Krumeich, F.; Hauert, R.; Stewart, J.A.; Curulla Ferré, D.; Pérez-Ramírez, J. Role of zirconia in indium oxide-catalyzed CO_2 hydrogenation to methanol. *ACS Catal.* **2020**, *10*, 1133–1145.
17. Martin, O.; Martín, A.J.; Mondelli, C.; Mitchell, S.; Segawa, T.F.; Hauert, R.; Drouilly, C.; Curulla-Ferré, D.; Pérez-Ramírez, J. Indium oxide as a superior catalyst for methanol synthesis by CO_2 hydrogenation. *Angew. Chem. Int. Ed.* **2016**, *55*, 6261–6265.
18. Yang, C.; Pei, C.; Luo, R.; Liu, S.; Wang, Y.; Wang, Z.; Zhao, Z.-J.; Gong, J. Strong electronic oxide–support interaction over $\text{In}_2\text{O}_3/\text{ZrO}_2$ for highly selective CO_2 hydrogenation to methanol. *J. Am. Chem. Soc.* **2020**. [[CrossRef](#)]
19. Rui, N.; Zhang, F.; Sun, K.; Liu, Z.; Xu, W.; Stavitski, E.; Senanayake, S.D.; Rodriguez, J.A.; Liu, C.-J. Hydrogenation of CO_2 to methanol on a $\text{Au}^{\delta+}-\text{In}_2\text{O}_{3-x}$ catalyst. *ACS Catal.* **2020**, *10*, 11307–11317.
20. Rui, N.; Sun, K.; Shen, C.; Liu, C.-J. Density functional theoretical study of $\text{Au}_4/\text{In}_2\text{O}_3$ catalyst for CO_2 hydrogenation to methanol: The strong metal-support interaction and its effect. *J. CO₂ Util.* **2020**, *42*, 101313.
21. Shi, Z.; Tan, Q.; Wu, D. A novel core–shell structured CuIn@SiO_2 catalyst for CO_2 hydrogenation to methanol. *AICHE J.* **2019**, *65*, 1047–1058.
22. Shi, Z.; Tan, Q.; Tian, C.; Pan, Y.; Sun, X.; Zhang, J.; Wu, D. CO_2 hydrogenation to methanol over Cu-In intermetallic catalysts: Effect of reduction temperature. *J. Catal.* **2019**, *379*, 78–89.
23. Bavykina, A.; Yarulina, I.; Al Abdulghani, A.J.; Gevers, L.; Hedhili, M.N.; Miao, X.; Galilea, A.R.; Pustovarenko, A.; Dikhtierenko, A.; Cadiau, A.; et al. Turning a methanation Co catalyst into an In-Co methanol producer. *ACS Catal.* **2019**, *9*, 6910–6918.
24. Ye, J.; Liu, C.-J.; Mei, D.; Ge, Q. Methanol synthesis from CO_2 hydrogenation over a $\text{Pd}_4/\text{In}_2\text{O}_3$ model catalyst: A combined DFT and kinetic study. *J. Catal.* **2014**, *317*, 44–53.
25. Rui, N.; Wang, Z.; Sun, K.; Ye, J.; Ge, Q.; Liu, C.-J. CO_2 hydrogenation to methanol over $\text{Pd}/\text{In}_2\text{O}_3$: Effects of Pd and oxygen vacancy. *Appl. Catal. B* **2017**, *218*, 488–497.
26. Frei, M.S.; Mondelli, C.; García-Muelas, R.; Kley, K.S.; Puértolas, B.; López, N.; Safonova, O.V.; Stewart, J.A.; Curulla Ferré, D.; Pérez-Ramírez, J. Atomic-scale engineering of indium oxide promotion by palladium for methanol production via CO_2 hydrogenation. *Nat. Commun.* **2019**, *10*, 3377.
27. Cai, Z.; Dai, J.; Li, W.; Tan, K.B.; Huang, Z.; Zhan, G.; Huang, J.; Li, Q. Pd supported on MIL-68(In)-derived In_2O_3 nanotubes as superior catalysts to boost CO_2 hydrogenation to methanol. *ACS Catal.* **2020**, *10*, 13275–13289.
28. Wang, J.; Sun, K.; Jia, X.; Liu, C.-J. CO_2 hydrogenation to methanol over $\text{Rh}/\text{In}_2\text{O}_3$ catalyst. *Catal. Today* **2020**. [[CrossRef](#)]
29. Jia, X.; Sun, K.; Wang, J.; Shen, C.; Liu, C.-J. Selective hydrogenation of CO_2 to methanol over $\text{Ni}/\text{In}_2\text{O}_3$ catalyst. *J. Energy Chem.* **2020**, *50*, 409–415.
30. Sun, K.; Rui, N.; Zhang, Z.; Sun, Z.; Ge, Q.; Liu, C.-J. A highly active $\text{Pt}/\text{In}_2\text{O}_3$ catalyst for CO_2 hydrogenation to methanol with enhanced stability. *Green Chem.* **2020**, *22*, 5059–5066.
31. Han, Z.; Tang, C.; Wang, J.; Li, L.; Li, C. Atomically dispersed Pt^{n+} species as highly active sites in $\text{Pt}/\text{In}_2\text{O}_3$ catalysts for methanol synthesis from CO_2 hydrogenation. *J. Catal.* **2020**. [[CrossRef](#)]
32. Su, J.; Wang, D.; Wang, Y.; Zhou, H.; Liu, C.; Liu, S.; Wang, C.; Yang, W.; Xie, Z.; He, M. Direct conversion of syngas into light olefins over zirconium-doped indium(III) oxide and SAPO-34 bifunctional catalysts: Design of oxide component and construction of reaction network. *ChemCatChem* **2018**, *10*, 1536–1541.
33. Zhu, H.; Wang, X.; Yang, F.; Yang, X. Template-free, surfactantless route to fabricate In(OH)_3 monocrystalline nanoarchitectures and their conversion to In_2O_3 . *Cryst. Growth Des.* **2008**, *8*, 950–956.
34. Luo, M.-F.; Yan, Z.-L.; Jin, L.-Y.; He, M. Raman spectroscopic study on the structure in the surface and the bulk shell of $\text{Ce}_x\text{Pr}_{1-x}\text{O}_{2-\delta}$ mixed oxides. *J. Phys. Chem. B* **2006**, *110*, 13068–13071. [[PubMed](#)]
35. Jiang, X.; Nie, X.; Gong, Y.; Moran, C.M.; Wang, J.; Zhu, J.; Chang, H.; Guo, X.; Walton, K.S.; Song, C. A combined experimental and DFT study of H_2O effect on $\text{In}_2\text{O}_3/\text{ZrO}_2$ catalyst for CO_2 hydrogenation to methanol. *J. Catal.* **2020**, *383*, 283–296.

36. Cui, Y.; Xu, L.; Chen, M.; Lian, X.; Wu, C.-e.; Yang, B.; Miao, Z.; Wang, F.; Hu, X. Facilely fabricating mesoporous nanocrystalline Ce–Zr solid solution supported CuO-based catalysts with advanced low-temperature activity toward CO oxidation. *Catal. Sci. Technol.* **2019**, *9*, 5605–5625.
37. Gonçalves, A.; Puna, J.F.; Guerra, L.; Campos Rodrigues, J.; Gomes, J.F.; Santos, M.T.; Alves, D. Towards the development of syngas/biomethane electrolytic production, using liquefied biomass and heterogeneous catalyst. *Energies* **2019**, *12*, 3787. [CrossRef]
38. Gao, P.; Dang, S.; Li, S.; Bu, X.; Liu, Z.; Qiu, M.; Yang, C.; Wang, H.; Zhong, L.; Sun, Y. Direct production of lower olefins from CO₂ conversion via bifunctional catalysis. *ACS Catal.* **2018**, *8*, 571–578.
39. Frei, M.; Mondelli, C.; Short, M.; Pérez-Ramírez, J. Methanol as a hydrogen carrier: Kinetic and thermodynamic drivers for its CO₂-based synthesis and reforming over heterogeneous catalysts. *ChemSusChem* **2020**, *13*, 1–9.

Publisher's Note: MDPI stays neutral with regard to jurisdictional claims in published maps and institutional affiliations.



© 2020 by the authors. Licensee MDPI, Basel, Switzerland. This article is an open access article distributed under the terms and conditions of the Creative Commons Attribution (CC BY) license (<http://creativecommons.org/licenses/by/4.0/>).